Bioinspired, Multifunctional, Active Whisker Sensors for Tactile Sensing of Mobile Robots

Zhiqiang Yu, *Member, IEEE*, Yue Guo, Jiaji Su, Qiang Huang, *Fellow, IEEE*, Toshio Fukuda, *Life Fellow, IEEE*, Changyong Cao, *Member, IEEE*, and Qing Shi, *Senior Member, IEEE*

***Abstract*—Whiskers of some animals, such as rats and cats, can actively sense stimuli from their surrounding environment. Such a capability is attractive for intelligent mobile robots. However, an artificial whisker with similar abilities has not been fully developed so that the robots acquire their surrounding environment information in an active approach such as rats. In this paper, we propose a new bioinspired active whisking tactile sensor (MAWS) capable of sensing the distance, shape, size, and orientation of caves and environmental conditions. Two orthogonally distributed linear Hall sensors are mounted beneath a circular permanent magnet for spatial localization of the whisker. The whisker is then actuated and controlled by an array of nine electromagnetic coils by tuning the excitation current and phase sequence. Conical pendulum and bidirectional sweeping strategies were designed to mimic the simultaneous perception behavior of rats. A reactive obstacle avoidance experiment was also conducted to evaluate the performance of the proposed MAWS installed on a mobile robot.**

***Index Terms*—Active sensing, bioinspired tactile sensors, distance perception, reactive obstacle avoidance, shape reconstruction.**

I. Introduction

PERCEPTION is critically important for mobile robots to sense their surrounding environments to perform effective and accurate control and responses. Over the decades, various functional sensors have been developed to enhance the perception ability of robots [1]–[4]. Recently, flexible tactile sensors have enabled robots to carry out delicate tasks due to the compact and compliant feedback system for contact force [5], [6]. However, these kinds of epidermal tactile sensors are challenging to provide tactile sensation through active sensing, thereby limiting their applications for reactive obstacle avoidance of mobile robots.

It is known that certain nocturnal animals, such as rats and whales, in nature have evolved effective biological tactile systems to actively sense complex stimuli and generate immediate reactions to them. For instance, rats can run fast in a dark environment to sense their surrounding environments or search for food by sweeping their facial whiskers (or vibrissae) [7]. Their whiskers are independently moved by the follicle-sinus complex (FSC) located beneath the facial skin [8]. Recent research revealed that the tactile whiskers of rats have high sensitivity, specificity, and short response time as active systems and can detect a variety of features, such as shape, location, orientation, surface texture, and radial distance by actively whisking their facial whiskers[9]–[11].

Inspired by the sensing mechanism of rat FSC (Fig. 1(a)), many active artificial whisker sensors have been designed for robots to extract important environmental information [12]–[14]. Compared with traditional passive sensing whiskers[15], active whiskers are able to improve the detection efficiency of unknown environments by extending the perception area through sweeping. However, most reported designs employ electric motors or robots as actuators, resulting in a bulky and heavy structure. Although the piezoelectric active sensor can retain a compact structure [16], the required high voltage, intrinsic hysteresis, and limited sweep amplitude have hindered its broad applications in mobile robots.

To realize a close-range interaction with the surrounding environment, distance estimation plays a key role in the reactive obstacle avoidance and navigation of robots [17]. For the past few years, laser range finders or binocular vision have been widely adopted by robots to provide a remote interaction capability with the environment [18], [19]. However, it is still challenging for robots to achieve a close-range interaction with their surrounding environment, especially in a dark environment. Interestingly, natural animals such as rats can interact closely with their surrounding environment through their facial whiskers [9], [10] even in a dark environment. Therefore, the bioinspired whisker sensors used to calculate the distance have been widely studied and have made great progress [11], [13].

In this work, we have developed a multifunctional active whisker sensor (MAWS) that can be fully printed for building a robotic tactile sensing system (Fig. 1(b)). It is the first highly integrated artificial whisker sensor that can simultaneously sense

Manuscript received 23 February 2022; accepted 24 June 2022. Date of publication 15 July 2022; date of current version 26 July 2022. This letter was recommended for publication by Associate Editor M. Gauthier and Editor A. Banerjee upon evaluation of the reviewers' comments. This work was supported in part by the National Natural Science Foundation of China under Grant U2013208 and in part by the China National Postdoctoral Program for Innovative Talents under Grant BX20200054. *(Corresponding authors: Zhiqiang Yu; Changyong Cao.)*

Zhiqiang Yu, Yue Guo, Qiang Huang, Toshio Fukuda, and Qing Shi are with the Beijing Advanced Innovation Center for Intelligent Robots and Systems, School of Mechatronical Engineering and Key Laboratory of Biomimetic Robots and Systems, Ministry of Education, Beijing Institute of Technology, Beijing 100081, China (e-mail: yzq_09@163.com; yueguo@bit.edu.cn; qhuang@bit.edu.cn; tofukuda@nifty.com; shiqing@bit.edu.cn).

Jiaji Su and Changyong Cao are with the Laboratory for Soft Machines and Electronics, Department of Mechanical & Aerospace Engineering, Case Western Reserve University, Cleveland, OH 44106 USA (e-mail: jiaji.su@case.edu; ccao@case.edu).

This letter has supplementary downloadable material available at https://doi.org/10.1109/LRA.2022.3191172, provided by the authors.

Digital Object Identifier 10.1109/LRA.2022.3191172

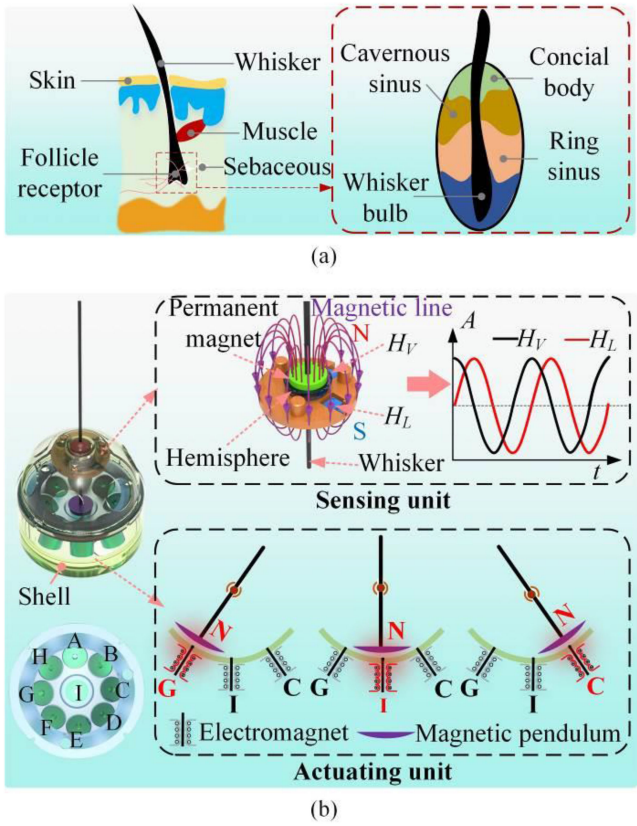

Fig. 1. Bioinspired multifunctional active whisker sensor (MAWS). (a) Schematic of the FSC of rats. (b) Schematic illustration of MAWS: the sensing and actuating units, and their structural configuration.

the shape, distance, size, and orientation information in an active manner. The MAWS is able to capture the key functions of the FSC system of rats. It has integrated two orthogonally distributed linear Hall sensors to mimic the follicle receptor of rats to obtain the real-time spatial movement information of the whisker. Nine electromagnetic coils were employed to actuate the active whisker to generate a rhythmic movement, similar to the muscle in the FSC. Two basic active sweeping modes (*i.e.*, conical pendulum mode and bidirectional sweeping mode) were designed and implemented by tuning the excitation current and phase sequence of the electromagnetic coils. An in-house characterization system was also designed and prototyped to evaluate the performance of the MAWS in characterizing the shape, distance, size, and orientation of the environment. Finally, the MAWS was integrated into an autonomous ground vehicle (AGV) to test its performance in reactive obstacle avoidance. With the assistance of the MAWS, the AGV successfully avoided the collision and demonstrated the effectiveness and applicability of the proposed MAWS for robotics.

II. Methods

A. Prototype Design and Working Mechanism of the MAWS

Rats can run at a high speed in darkness without colliding with any surrounding obstacles by using their whiskers. Fig. 1(a) depicts the major anatomical structure of a rat whisker follicle. The innervation regions are used to transduce mechanical signals from the whisker [20]. The musculature can actively control the motions of whiskers. Inspired by the rat whisker, we propose a new MAWS (Fig. 1(b)) that is able to measure the shape, distance, size, and orientation information of environments. The MAWS consists of a sensing unit and an actuating unit. The sensing unit has two orthogonally distributed linear Hall sensors H_V and H_L (WSH138, Aoweziic), a 3D-printed ball bearing and its holder, and a hollow cylinder NdFeB permanent magnet (Φ 8 mm × 3 mm). The permanent magnet is placed with its "N" pole towards along the whisker (Fig. 1(b), upper), embedded in the bearing. As the whisker sweeps, the permanent magnet also moves with the whisker. The deflection of the permanent magnet produces a changing magnetic field, which is instantaneously recorded by the linear Hall sensors. According to the measured signal by the Hall sensors, the movement state and position of the whisker tip can be obtained in a real-time manner.

The actuation unit is mainly composed of a carbon fiber (whisker), a magnetic pendulum, electromagnetic coils and a spherical shell (Fig. 1(b), below). A thin NdFeB permanent magnet (Φ 9 mm×1 mm) was mounted at the end of the whisker to form a pendulum structure, and the "N" pole of the magnet pointed to the center of the shell structure of the actuating unit. Nine electromagnetic coils (Φ 8 mm×9.5 mm) were firmly attached to the internal surface of the shell, and 1 mm thick cylindrical silicon iron was implanted into the electromagnetic coils to enhance the produced magnetic field. Each coil was assembled with 3760 turns of varnished wire (Φ 0.2 mm), and the produced polarity and magnitude of the magnetic field can be independently tuned by a dual full-bridge driver L298, which can provide a current up to 4 A. Once the whisker bridges the sensing and actuating unit through the magnetic pendulum and the ball bearing, the pendulum can drive the whisker to generate a preset movement by programming the power sequence, polarity, and frequency of the electromagnetic coils.

B. Control Strategies

To mimic the active sensing behaviors of rats, we propose two control strategies to generate the bidirectional sweeping motion and the conical pendulum motion of the MAWS (Fig. 2). The bidirectional sweeping mode is to move the pendulum between the boundary and center electromagnetic coils (Fig. 2(a)), while the conical pendulum mode is to move the pendulum along the peripheral circle line formed by the boundary electromagnetic coils (Fig. 2(b)). Both modes can be used to sense the surrounding environment in an active method.

As shown in Fig. 2(a), the bidirectional sweeping of the whisker is achieved by sequentially powering linearly distributed electromagnetic coils (*e.g.,* G-I-C). Considering that the MAWS can be randomly positioned, we must first find the pendulum and then perform its bidirectional sweeping. Therefore, we initially power all the surrounding coils to generate a repulsive mode while keeping the central coil in an attractive mode, leading to the restoring of the pendulum to the central coil position. Once the pendulum reaches the center coil, a series of time-resolved signals can be applied to drive the whisker to

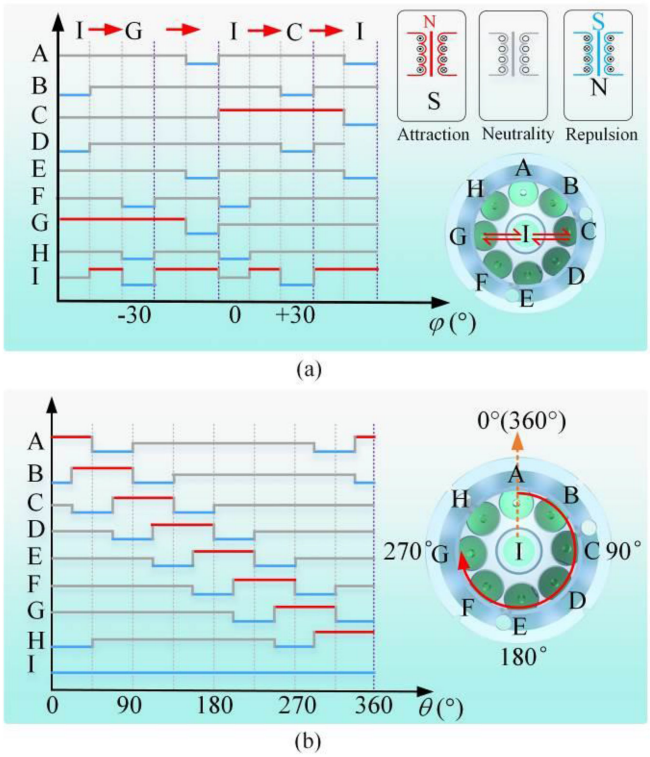

Fig. 2. Two working modes and related actuation mechanism of the MAWS. The red, blue, and gray lines represent the attraction, repulsion, and neutrality states, respectively. (a) Bidirectional sweeping mode. (b) Conical pendulum mode.

perform swiping. For clarity, we take the bidirectional sweeping among the three coils G, I, and C to describe the active whisking behavior. Fig. 2(a) illustrates the energizing state of the nine electromagnetic coils over time. Depending on the energized state, each electromagnetic coil consists of three basic states in terms of the magnetic pendulum: attraction, repulsion, and neutrality. The red line indicates the attractive state, while the blue line represents the repulsive state. The gray line is the power-off state, and no magnetic field is generated (neutrality). To avoid wandering of the whisker during its sweeping mode, the adjacent coils were set to a repulsive state when the magnetic pendulum entered the desired position (*e.g.*, Fig. 2(a), 40∼60 ms). Furthermore, a pre-attractive magnetic field was also used to guide the motion of the magnetic pendulum as it moved away from its previous position (*e.g.*, Fig. 2(a), 60∼80 ms).

To generate a conical pendulum motion of the MAWS, we designed a rotating electromagnetic field to guide the pendulum by sequentially powering the electromagnetic coils from A to H (Fig. 2(b)). To accurately localize the magnetic pendulum, three electromagnetic coils were treated as one unit to generate the repulsion-attraction-repulsion complex, while the others were kept in a neutral state. In this complex, the middle attraction coil is used to initialize the pendulum, while the adjacent electromagnetic coils are used to balance the resultant force formed by the inertia force, the fractional force between the pendulum and the

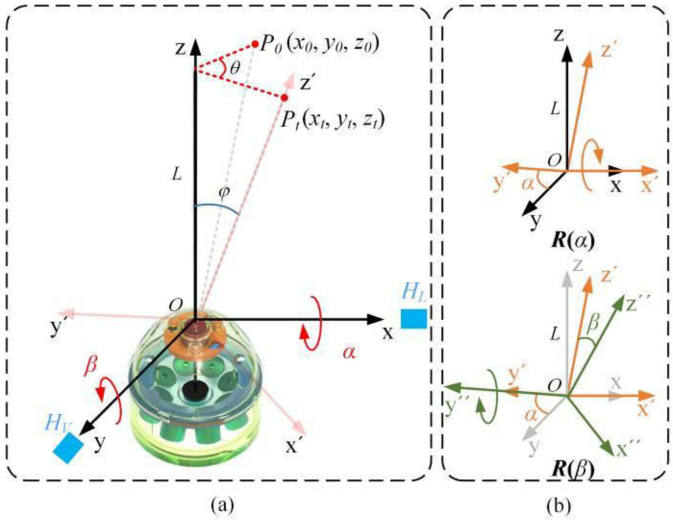

Fig. 3. Schematic illustration of the spatial positioning mechanism for MAWS. (a). Spatial positioning based on α and β. (b) Transfer matrices calculation.

MAWS shell, and other external disturbances. The central electromagnetic coil (I) maintains a repulsive state to the pendulum in this operation process, thereby constraining the pendulum to generate conical sweeping movement. To smoothly control the conical pendulum process, a periodic A-AB-B- …, …-H-HA-A powering sequence is utilized to further subdivide the electromagnetic field. It is noted that the conical pendulum moving direction can also be reversed by simply changing the excitation sequence of the coils. The conical pendulum speed and acceleration can be adjusted by tuning the electromagnetic field through the applied electric current. In comparison of the two active whisking modes, it can be concluded that the bidirectional sweeping mode possesses a high potential for reactive obstacle avoidance of mobile robots due to its short-stroke, while the conical pendulum whisking mode is suitable for effectively capturing the graphical information of surrounding environments.

C. Sensing Theory

Fig. 3(a) illustrates the positioning mechanism of the MAWS. The carbon fiber is assumed to be rigid due to its high Young's modulus [21], and no rotation occurs on the z-axis. Thus, when the whisker moves from position $\mathbf{P_0}$ (x_0, y_0, z_0) to position $\mathbf{P_t}$ (x_t, y_t, z_t), $\mathbf{P_t}$ can be represented by:

$$\mathbf{P_t} = \mathbf{R_y}(\beta)\mathbf{R_x}(\alpha)\mathbf{P}_0 \tag{1}$$

where α and β are the rotation angles along the x-axis and y-axis, respectively. $\mathbf{R_y}$ and $\mathbf{R_x}$ are transfer matrices and can be obtained by rotating the coordinate axis (Fig. 3(b)). Therefore, $\mathbf{P_t}$ (x_t, y_t, z_t) can be represented as:

$$\begin{pmatrix} x_t \\ y_t \\ z_t \end{pmatrix} = \begin{pmatrix} \cos\beta & 0 & -\sin\beta \\ 0 & 1 & 0 \\ \sin\beta & 0 & \cos\beta \end{pmatrix} \begin{pmatrix} \cos\alpha & \sin\alpha & 0 \\ -\sin\alpha & \cos\alpha & 0 \\ 0 & 0 & 1 \end{pmatrix} \begin{pmatrix} x_0 \\ y_0 \\ z_0 \end{pmatrix} \tag{2}$$

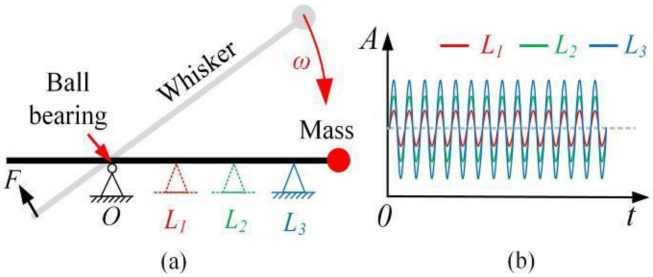

Fig. 4. Schematic illustration of the distance perception. (a) Forced vibration of the MWAS. (b) Vibration amplitude increase with the detection distance.

Therefore, once α and β are known, the spatial position of the whisker in real time can be calculated by (2). $\mathbf{P_t}$ can also be expressed by φ and θ in the original coordinate as:

$$x_t = L \cdot \sin\varphi \cdot \cos\theta \tag{3}$$

$$y_t = L \cdot \sin\varphi \cdot \sin\theta \tag{4}$$

$$z_t = L \cdot \cos\varphi \tag{5}$$

where L is the length of the whisker, φ is the swing angle, and θ is the azimuth angle. By combining (1) to (5), we can obtain φ and θ by:

$$\varphi = \cos^{-1}(\cos\alpha \cdot \cos\beta) \tag{6}$$

$$\theta = \cos^{-1}\left(\frac{\sin\beta}{\sin\varphi}\right) \tag{7}$$

If M_V and M_L denote the recorded intensity of the magnetic field for H_V and H_L, respectively, the variations in α and β can be expressed as a function of M_V and M_L. Therefore, we can accurately calculate α and β through the relationship between M_V and M_L. Once we acquire α and β, the arbitrary spatial position of the whisker can be calculated by (6) and (7). This spatial positioning ability enables MAWS to be used for characterizing the shape, size, and orientation of holes.

D. Distance Acquisition Strategies

As shown in Fig. 4, we propose a distance acquiring method based on the forced vibration, in which the forced vibration of the whisker was actuated by electromagnetic coils. When the obstacles are placed at different distances away from the MAWS, the vibration amplitude can be expressed by:

$$A = \frac{f}{|\omega_0^2 - \omega^2|} \tag{8}$$

where A is the amplitude, ω_0 is the intrinsic vibration frequency, ω is the forced frequency, and f is the result of F/m. F is the driving force from the powered electromagnetic coils, and m is the equivalent mass of the whisker. Based on the resonant frequency of a simply supported beam [22], we know that ω_0 is related to L. Therefore, we can obtain the corresponding A under different L, i.e., the closer the obstacles are to the MAWS, the larger the value A is (Fig. 4(b)).

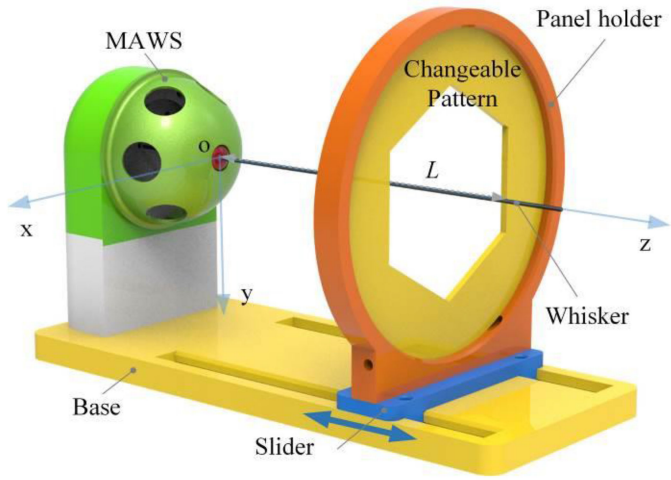

Fig. 5. Prototype of the characterization system for MAWS.

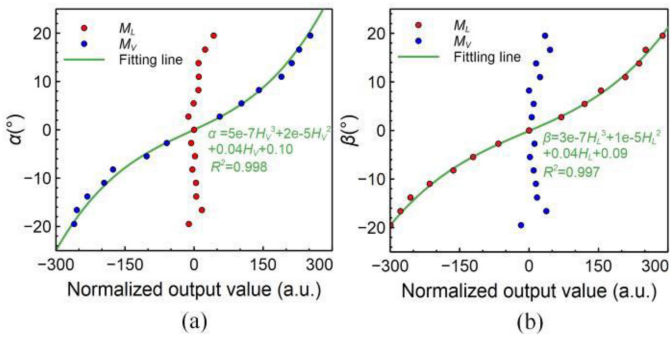

Fig. 6. Calibration of the linear Hall sensor. (a) and (b) depict the correlation between α-M_L and β-M_V, respectively.

III. Experiments and Results

A. Characterization System

To verify the performance of the proposed MAWS, we also designed a 3D-printed characterization system (Fig. 5). It consists of an MAWS, a changeable panel with different patterns, and a panel holder fixed on a slider to adjust the distance. The changeable panel is used to verify the active sensing capabilities of shape, size, and orientation of the MAWS, while the slider is designed to verify the distance sensing performance of the MWAS. The center of the ball bearing is coaxial with the changeable patterns, as shown in Fig. 5.

B. Calibration of Linear Hall Sensors

Prior to characterizing the performance of the MAWS, we first calibrated the linear Hall sensors. This is an essential step to obtain the relationship between α-M_V and β-M_L. Here, we carried out bidirectional sweeping along *xoz* and *yoz* planes and set $L = 105$ mm to calculate the values of α and β. After completing one sweeping cycle, we normalized the raw data to be zero-centered and plotted the curves of α-M_V and β-M_L (Fig. 6). The M_V (M_L) varies greatly as the whisker sweeps in the *yoz* (*xoz*) plane, while the M_L (M_V) is almost negligible. This

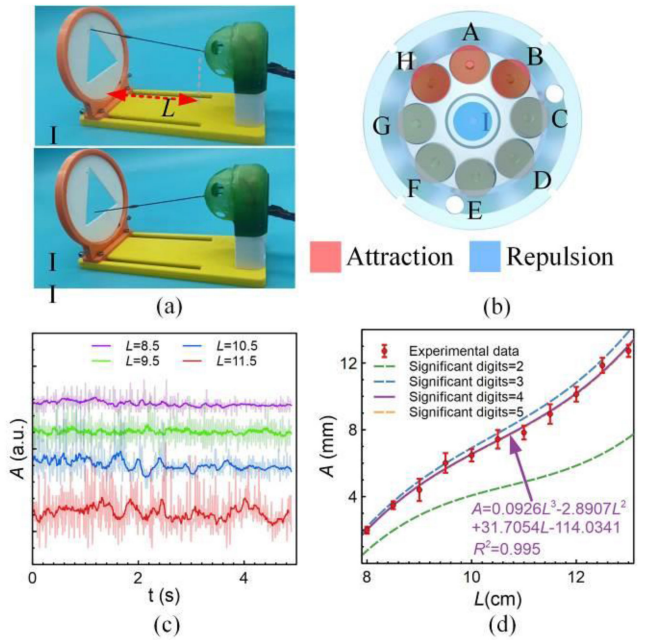

Fig. 7. Distance perception. (a) Experimental setup. (b) Powering state distribution of the electromagnetic coils. (c) Typical time-resolved A under different L. (d) Fitted A-L curves under different significant digits.

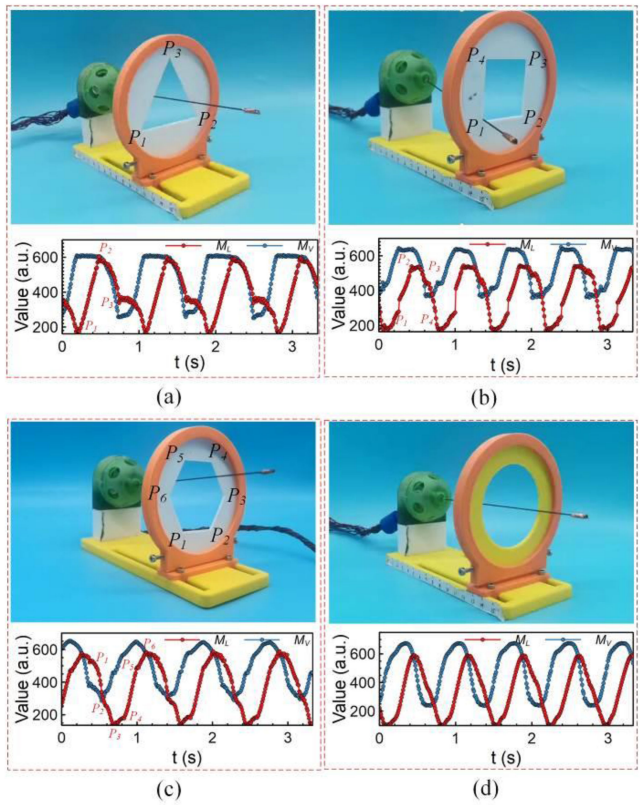

Fig. 8. Shape characterization: experimental setup and measured signals. (a) Triangle. (b) Square. (c) Polygon. (d) Circle.

indicates that α and β can be independently expressed by M_V and M_L. We obtain the correlation between α-M_V by fitting the output data as $\alpha = 5\times10^{-7}M_V{}^3+2\times10^{-5}M_V{}^2+0.04M_V+0.10$ ($R^2 = 0.998$). Similarly, the correlation between β-M_L is also obtained as $\beta = 3\times10^{-7}M_L{}^3+1\times10^{-5}M_L{}^2+0.04M_L+0.09$ ($R^2 = 0.997$). Notably, the M_V and M_L demonstrate a quasi- linear correlation with α and β. Therefore, α and β can be calculated by the obtained M_V and M_L based on the fitted linear equation $F(x) = 0.04x + 0.1$, where x represents the M_V or M_L.

C. Distance Perception

Fig. 7(a) demonstrates the experimental setup for verifying the performance of the MAWS on acquiring distance. A panel with a triangle pattern was treated as an obstacle in the environment. To provide the forced motion of the whisker, coils H, A, and B were switched on-off at a frequency of 4 Hz (Fig. 7(b), Movies S1). The typical time-resolved A curves at different L values over time are shown in Fig. 7(c). The light color lines depict the real-time variations of A, while the dark lines demonstrate the slide average performance of A. We can see that the maximum A increases as L lengthens. To acquire a property sampling frequency of the Hall sensor, the maximum vibration frequency of the whiskers was calculated based on the time-resolved A curves at different L. By taking the Fourier transform of the A curves in Fig. 7(c), the maximum vibration frequency is obtained as 100 Hz@L = 105 mm.

Considering that the standard response bandwidth of the employed Hall sensor is 23 kHz, which is far higher than the needed sampling frequency, we finally set the sampling frequency at 500 Hz. Notably, the sampling frequency can be tuned to megahertz to match the utmost bandwidth of the Hall sensor by tuning the clock division of the ADC (analog to digital converter).

The maximum vibration amplitudes of the typical time-resolved A curves were extracted from Fig. 7(c) and plotted in Fig. 7(d). To obtain the accurate relation between A and L, we conduct 5 experiments at each specific length. Their average amplitude of these 5 experiments was used as the amplitude of the specific distance L. Moreover, the significant digits of the A-L function coefficients were also analyzed. We can see that the A-L curves tend to overlap as the number of significant digits increases and are almost overlapped when the number of significant digits reaches 4. Therefore, we obtain the A-L function by fitting the experimental data as $A = 0.0926L^3$-$2.8907L^2+31.7054L$-114.0341 ($R = 0.995$). The mean squared error (MSE) of the obtained A-L function was also calculated as 0.048 mm, which indicates the high accuracy of the obtained A-L function. Notably, once θ, φ and L are known based on M_V and M_L, the size, shape and orientation of the obstacles can be perceived.

D. Shape, Size and Orientation Perception

In a dark environment, rats can perceive whether the cave or an obstructed environment is suitable for travel based on the shape and size detected by their whiskers [7]. To mimic their perception behavior, several 3D-printed panels with triangle, square, circle, and polygon shapes (Fig. 8) were prepared and assembled on

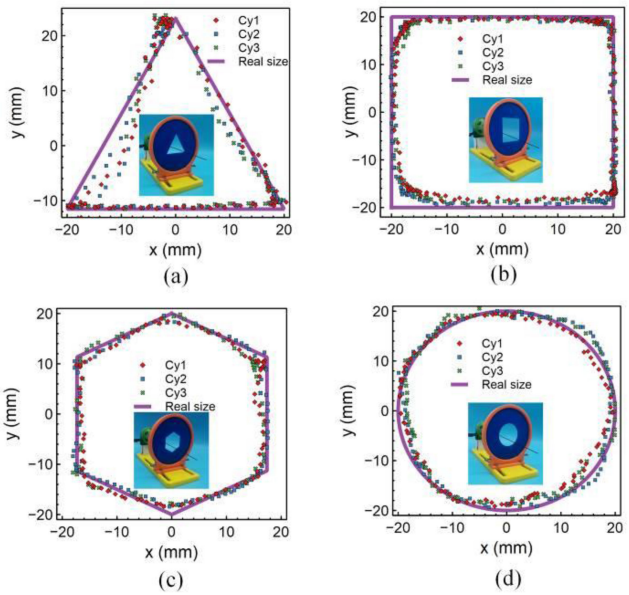

Fig. 9. Shape reconstruction of the patterns detected by MAWS. (a) Triangle. (b) Square. (c) Hexagon. (d) Circle.

the panel holder to verify the shape, size and orientation sensing capability of the MWAS (Movie S2).

Fig. 8 demonstrates the experimental setups and the captured data from H_L and H_V. We note that the time-resolved curves of M_L and M_V all demonstrate equal fragments as the edges of the detected panels, which can be used to teach the MAWS to understand and perceive the surrounding environment like a real rat. To gain a better understanding of the time-resolved curves of M_V and M_L, we highlighted the vertices of the triangle by P_1, P_2, and P_3 (Fig. 8(a)). As mentioned above, the

H_L (H_V) outputs a set of data M_L (M_V) only when the whisker generates a displacement projection on the x (y) axes (Fig. 5). Therefore, we obtained a sharp increase in the M_L when we execute an almost lateral whisking motion (from P_1 to P_2), as shown in Fig. 8(a). Correspondingly, the Hall sensor of H_V outputs an approximate constant during this process because no displacement projection occurs on the y-axes. From P_2 to P_3 and then back to P_1, the displacement projection of this process on the x-axes is unidirectional. Thus, H_L yields a continuous decline in the M_L. We can see that the unidirectional sweeping action of the whisker breaks the vertical symmetry of the obtained M_L curve, although the output data M_L and M_V tend to be vertically symmetric as the number of polygon sides increases.

To verify the shape reconstruction ability of the MAWS, four panels with different shapes (*i.e.,* triangle, square, hexagon and circle) were mounted on the panel holder, as the inset image shown in Fig. 9. The real size (side length) of the changeable triangle, rectangle and hexagon pattern is 40 mm, 40 mm, and 20 mm, respectively, while the real diameter of the circular pattern is 40 mm. We conduct the shape reconstruction experiment while the slider is 105 mm away from the MAWS.

Three cycles of the time-resolved M_V and M_L data of each pattern were extracted and converted to the real size and shape of the detected patterns based on (2), as demonstrated in Fig. 9. Interestingly, the triangle pattern obtains a relatively accurate shape sensing at the vertices compared to the other patterns. By carefully checking the shape construction movies of the triangle (Movie S2), we found that a backswing phenomenon occurred at the vertices of the triangle. We attribute the backswing phenomenon to the elastic collision between the whisker and the contour of the triangle pattern approaching the vertices. During this elastic collision process, the acute angle property constrains the movement of the whisker and yields out the vertices position of the detected triangle pattern. This explains why we collected more contour data at the vertices of the reconstructed patterns. The constraint effect weakened and disappeared with the increase in the interior angles ($>90°$) of the detected patterns and thus introduced the shape estimation error, as shown in Fig. 9(b) and 9(c).

Overall, the detected pattern can be reconstructed efficiently ($\sim$0.88 s) based on the conical whisking of the whisker. The reconstructed pattern shape also matches the real pattern well to a large extent, although the results are not satisfactory at some vertices of the detected patterns due to the bounce effect between the whisker and detected patterns. In practice, the bouncing impacts on shape reconstruction can be overcome by changing the conical pendulum mode into a sweeping mode. In the sweeping mode, the real contour of the pattern vertices can be obtained even though bouncing occurs. This is because the real contour can be obtained at the moment of contact between the whisker and contour of the patterns.

To quantitatively evaluate the reconstruction accuracy of the detected pattern size and shape, we performed an error analysis based on the Hausdorff distance [23]. The reconstructed shape contour points and the real shape contour points were used as two groups of point sets for calculating the pattern shape estimation error. The shape estimation error corresponding to the four patterns was calculated and is demonstrated in Fig. 10. Notably, the reconstructed pattern sizes match well with their real dimensions. The shape estimation error tends to occur on the vertices or the curved contour of the *detected* patterns. The pattern shape estimation error varies with the detected cycles and yields a maximum shape estimation error lower than 4 mm. This maximum shape estimation error is tolerable when considering the high shape reconstruction efficiency ($\sim$0.88 s).

Considering the impact of time delay on the reconstruction accuracy of pattern shape and size, the time delay between acquiring the raw data from the two Hall sensors and the position calculation of the whisker was experimentally measured by using a timer function (*micros()*) of the Arduino board. By recording the system time before and after the position calculation equation, the time difference (time delay) is obtained at about 4 μs. Thus, the estimation error resulting from the time delay can be further calculated based on the sweeping frequency of the whisker. In Fig. 8(a), the conical pendulum sweeping frequency is 1.14 Hz (T = 0.88 s). The estimation errors δ_φ and δ_θ resulting from the time delays in φ and θ can be calculated as $0.39''$and $0.59''$respectively. Here, in view of $(\sin\varphi)_{\max} = \sin\delta_\varphi$, $(\cos\varphi)_{\max}$ = 1-$\cos\delta_\varphi$, $(\sin\theta)_{\max} = \sin\delta_\theta$, and $(\cos\theta)_{\max}$ = 1-$\cos\delta_\theta$, the maximum position estimation error at $L = 105$ mm in x, y and z can be calculated based on (3), (4), and (5) as δ_x

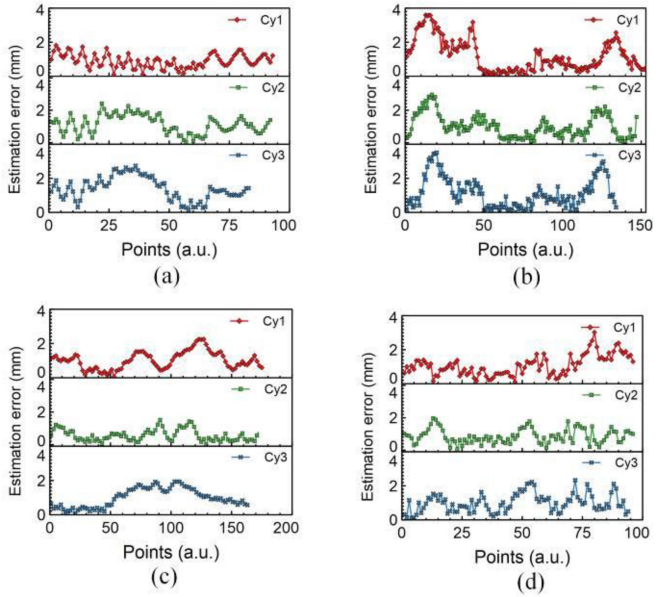

Fig. 10. Shape estimation error analysis of the detected patterns. (a) Triangle. (b) Square. (c) Hexagon. (d) Circle.

$= L{\cdot}\sin(\delta_\varphi){\cdot}(1\text{-}\cos\delta_\theta) = 3.1{\times}10^{-18}$ mm, $\delta_y = L{\cdot}\sin\delta_\varphi{\cdot}\sin\delta_\theta = 1.47{\times}10^{-11}$ mm, $\delta_z = L{\cdot}(1\text{-}\cos\delta_\varphi) = 5.72{\times}10^{-12}$ mm. We can see that the position estimation error resulting from the time delay is insignificant and can be neglected. In terms of orientation, we can calculate it in a real-time manner based on the acquired θ from (7).

E. Reactive Obstacle Avoidance

To further verify the effectiveness and applicability of the designed MAWS, we carried out a reactive obstacle avoidance experiment by integrating it into a commercial AGV car (10×10 cm). It is driven by a dual DC geared motor without an encoder and is controlled by an ATmega328 processer, which is suitable for investigating the ideas proposed in this paper.

To verify the reactive obstacle avoidance capability of the MAWS, we built an orthogonal wall with an acrylic board (Fig. 11(a)) and left one wall fixed by the tape. Without the guidance of the MAWS, the AGV robot moved forward blindly and did not stop until it hit down the wall (Fig. 11(b)). We then mounted the MAWS on top of an AGV robot and switched the whisker to the bidirectional sweeping mode (Fig. 2(b)). The sweeping frequency was set as 0.67 Hz. The whisker was ∼150 mm in length, and the sweeping angle φ was set at ∼60°. The dual full-bridge driver L298 was supplied by an 8 V DC power and controlled by an ATmega2560 processer. The power consumption of each electromagnetic coil was ∼3.2 W. The acquired analog signal obtained from the linear Hall sensor was first processed by the ADC and then processed by a programmed reactive obstacle avoidance algorithm to generate the control commands. The generated control commands were transmitted to the AGV robot through a Bluetooth module. According to the collision steering experiment, we finally set the maximum movement speed of the AGV robot to 10 cm/s.

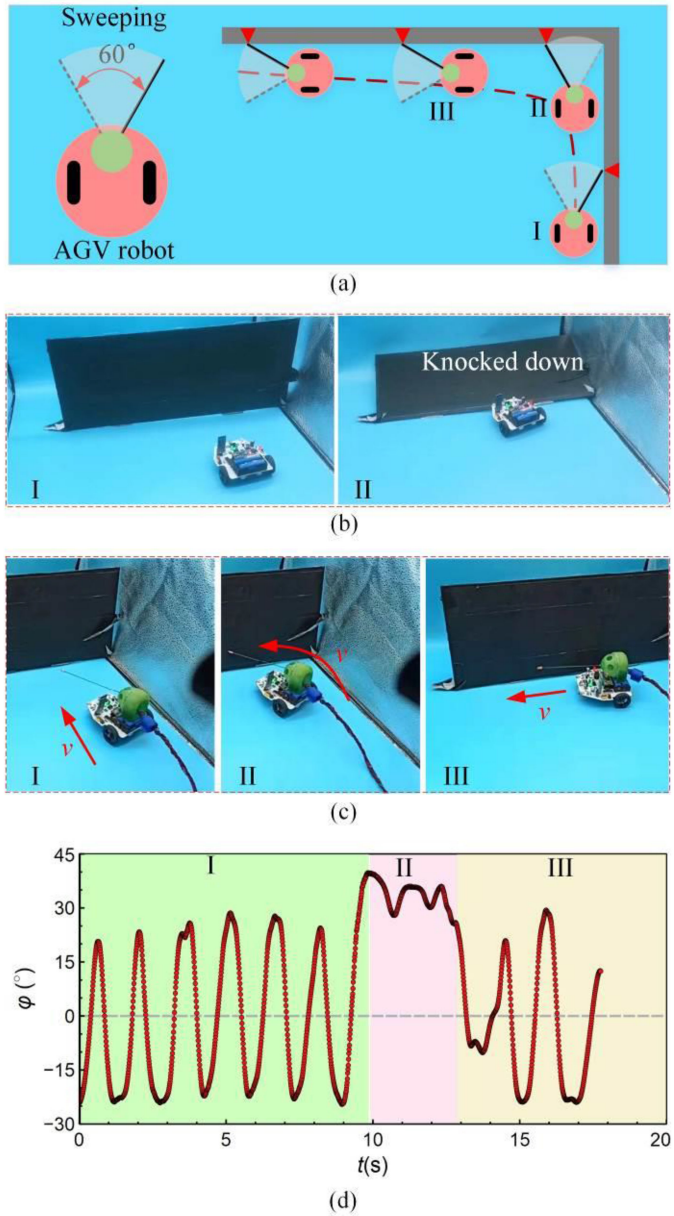

Fig. 11. Reactive obstacle avoidance experiment based on MAWS mounted on an AGV robot. (a) Schematic illustration of the experimental setup. AGV robot moving (b) without and (c) with a MAWS. (d) Time-resolved variation of φ during reactive obstacle avoidance.

Fig. 11(c) demonstrates the testing results of the reactive obstacle avoidance experiments after installing the MAWS (Movie S3). It can be seen that the AGV robot could successfully avoid possible collisions with walls. This process can be divided into three stages: approaching, perception, and avoidance. In brief, the AGV robot approached the wall (Fig. 11(c), I), and then the active sweeping whisker sensed the wall (Fig. 11(c), II). After that, the robot turned left and moved along the wall (Fig. 11(c), III) to avoid possible collision, similar to the rats reacting to the environment with their facial sweeping whiskers. To quantitatively analyze the collision avoidance process, a slide average approach was employed to smooth the acquired φ.

Fig. 11(d) demonstrates the time-resolved variations of φ during the reactive obstacle avoidance of the AGV robot.

IV. Conclusion

A bioinspired multifunctional active whisker sensor has been developed for mobile robots in graphic recognition and reactive obstacle avoidance. The new whisker sensor has two working modes, an active conical pendulum mode and bidirectional sweeping mode, by powering nine electromagnetic coils sequentially. A pair of orthogonally distributed linear Hall sensors were used to monitor the variation in the magnetic field of the permanent magnet mounted on the whisker. The variation in the magnetic field resulting from whisking has been successfully utilized to sense the distance, shape, size, and orientation of the obstacles in the surrounding environment. We also demonstrated the MAWS in an AGV robot to evaluate its performance in reactive obstacle avoidance for mobile robots. This research provides new designs and approaches in the development of multifunctional active tactile sensing systems for mobile robotic applications.

References

[1] T. Jin *et al.*, "Triboelectric nanogenerator sensors for soft robotics aiming at digital twin applications," *Nature Commun.*, vol. 11, no. 1, Oct. 2020, Art. no. 5381.

[2] G. Z. Yang *et al.*, "The grand challenges of science robotics," *Sci. Robot.*, vol. 3, no. 14, Jan. 2018, Art. no. eaar7650.

[3] S. I. Rich, R. J. Wood, and C. Majidi, "Untethered soft robotics," *Nature Electron.*, vol. 1, no. 2, pp. 102–112, 2018.

[4] S. Chen *et al.*, "Soft crawling robots: Design, actuation, and locomotion," *Adv. Mater. Technol.,* vol. 5, no. 2, 2020, Art. no. 1900837.

[5] U. Kim *et al.*, "Integrated linkage-driven dexterous anthropomorphic robotic hand," *Nature Commun.*, vol. 12, no. 1, Dec. 2021, Art. no. 7177.

[6] M. Liu *et al.*, "A star-nose-like tactile-olfactory bionic sensing array for robust object recognition in non-visual environments," *Nature Commun.,* vol. 13, no. 1, Jan. 2022, Art. no. 79.

[7] E. Chorev, P. Preston-Ferrer, and M. Brecht, "Representation of egomotion in rat's trident and E-row whisker cortices," *Nature Neurosci.,* vol. 19, no. 10, pp. 1367–1373, Oct. 2016.

[8] M. E. Diamond, M. von Heimendahl, P. M. Knutsen, D. Kleinfeld, and E. Ahissar, "'Where' and 'what' in the whisker sensorimotor system," *Nature Rev. Neurosci.*, vol. 9, no. 8, pp. 601–612, Aug. 2008.

[9] Y. Luo, C. S. Bresee, J. W. Rudnicki, and M. J. Z. Hartmann, "Constraints on the deformation of the vibrissa within the follicle," *PLoS Comput. Biol.*, vol. 17, no. 4, Apr. 2021, Art. no. e1007887.

[10] M. Adibi, M. E. Diamond, and E. Arabzadeh, "Behavioral study of whisker-mediated vibration sensation in rats," *Proc. Nat. Acad. Sci.*, vol. 109, no. 3, pp. 971–976, Jan. 2012.

[11] J. H. Solomon and M. J. Z. Hartmann, "Radial distance determination in the rat vibrissal system and the effects of Weber's law," *Philos. Trans. Roy. Soc. B: Biol. Sci.*, vol. 366, no. 1581, pp. 3049–3057, 2011.

[12] M. J. Pearson and M. Salman, "Active whisker placement and exploration for rapid object recognition," in *Proc. IEEE/RSJ Int. Conf. Intell. Robots Syst.*, 2019, pp. 672–677.

[13] N. H. Nguyen, T. D. Ngo, D. Q. Nguyen, and V. A. Ho, "Contact distance estimation by a soft active whisker sensor based on morphological computation," in *Proc. 8th IEEE RAS/EMBS Int. Conf. Biomed. Robot. Biomechatronics*, 2020, pp. 322–327.

[14] N. F. Lepora, M. Pearson, and L. Cramphorn, "TacWhiskers: Biomimetic optical tactile whiskered robots," in *Proc. IEEE/RSJ Int. Conf. Intell. Robots Syst.*, 2018, pp. 7628–7634.

[15] Y. Zhang, S. Yan, Z. Wei, X. Chen, T. Fukuda, and Q. Shi, "A small-scale, rat-inspired whisker sensor for the perception of a biomimetic robot: Design, fabrication, modeling, and experimental characterization," *IEEE Robot. Automat. Mag.*, early access, Jul. 7, 2022, doi: 10.1109/MRA.2022.3182870.

[16] F. Ju and S.-F. Ling, "Bioinspired active whisker sensor for robotic vibrissal tactile sensing," *Smart Mater. Structures*, vol. 23, no. 12, 2014, Art. no. 125003.

[17] G. C. H. E. de Croon, C. De Wagter, and T. Seidl, "Enhancing optical-flow-based control by learning visual appearance cues for flying robots," *Nature Mach. Intell.,* vol. 3, no. 1, pp. 33–41, Jan. 2021.

[18] W. Shao, H. Zhang, Y. Wu, and N. Sheng, "Application of fusion 2D lidar and binocular vision in robot locating obstacles," *J. Intell. Fuzzy Syst.,* vol. 41, pp. 4387–4394, 2021.

[19] A. Carballo, A. Ohya, and S. Yuta, "People detection using range and intensity data from multi-layered laser range finders," in *Proc. IEEE/RSJ Int. Conf. Intell. Robots Syst.*, 2010, pp. 5849–5854.

[20] P. Xu *et al.*, "A triboelectric-based artificial whisker for reactive obstacle avoidance and local mapping," *Research,* vol. 2021, pp. 1–10, 2021.

[21] S. Allen, G. A. Cooper, and R. M. Mayer, "Carbon fibres of high young's modulus," *Nature,* vol. 224, no. 5220, pp. 684–685, Nov. 1969.

[22] W. Weaver Jr. *et al.*, *Vibration Problems in Engineering*, 5th ed., W. Weaver Jr., S. P. Timoshenko, and D. H. Young, Eds, Chichester, U.K.: Wiley, 1990.

[23] D. P. Huttenlocher, G. A. Klanderman, and W. J. Rucklidge, "Comparing images using the Hausdorff distance," *IEEE Trans. Pattern Anal. Mach. Intell.*, vol. 15, no. 9, pp. 850–863, Sep. 1993.